1   **Homogeneous multifocal excitation for high-throughput super-resolution imaging**

2   Dora Mahecic[1,2]*, Davide Gambarotto[3], Kyle M. Douglass[1], Denis Fortun[4], Niccoló

3   Banterle[2,5], Maeva Le Guennec[3], Khalid Ibrahim[1], Pierre Gönczy[2,5], Virginie Hamel[3], Paul

4   Guichard[3], Suliana Manley[1,2]*

5

6

7   Affiliations

8   [1] Laboratory for Experimental Biophysics, Institute of Physics, Swiss Federal Institute of

9   Technology Lausanne (EPFL), Lausanne, Switzerland.

10   [2] Swiss National Centre for Competence in Research (NCCR) in Chemical Biology,

11   University of Geneva, Geneva, Switzerland.

12   [3] Department of Cell Biology, Sciences III, University of Geneva, Geneva, Switzerland.

13   [4] ICube, CNRS, University of Strasbourg, Illkirch, France.

14   [5] Swiss Institute for Experimental Cancer Research, School of Life Sciences, Swiss Federal

15   Institute of Technology Lausanne (EPFL), Lausanne, Switzerland.

16

17   *Corresponding authors: suliana.manley@epfl.ch; dora.mahecic@epfl.ch

18

Abstract

Super-resolution microscopies, which allow features below the diffraction limit to be resolved, have become an established tool in biological research. However, imaging throughput remains a major bottleneck in using them for quantitative biology, which requires large datasets to overcome the noise of the imaging itself and to capture the variability inherent to biological processes. Here, we develop a multi-focal flat illumination for field independent imaging (mfFIFI) module, and integrate it into an instant structured illumination microscope (iSIM). Our instrument extends the field of view (FOV) to >100x100 μm^2 without compromising image quality, and maintains high-speed (100 Hz), multi-color, volumetric imaging at double the diffraction-limited resolution. We further extend the effective FOV by stitching multiple adjacent images together to perform fast live-cell super-resolution imaging of dozens of cells. Finally, we combine our flat-fielded iSIM setup with ultrastructure expansion microscopy (U-ExM) to collect 3D images of hundreds of centrioles in human cells, as well as of thousands of purified *Chlamydomonas reinhardtii* centrioles per hour at an effective resolution of ~35 nm. We apply classification and particle averaging to these large datasets, allowing us to map the 3D organization of post-translational modifications of centriolar microtubules, revealing differences in their coverage and positioning.

Introduction

Super-resolution fluorescence techniques have enabled optical imaging beyond the diffraction limit. Two main illumination strategies are used to achieve super-resolution: wide-field illumination is typically used for single-molecule localization microscopies (SMLM) such as STORM[1] and PALM[2], while patterned illumination is typically used for methods such as structured illumination microscopy (SIM)[3,4] and stimulated emission depletion (STED)[5]. Initial implementations of these methods were relatively slow, in part due to the use of the time domain to separate single molecules (SMLM), the need to collect multiple images to cover Fourier space (SIM), or the scanning of a reduced excitation volume

2

45   (STED). In both wide-field and patterned illumination, the imaging throughput – defined as

46   the area imaged per time – can be increased by parallelizing the acquisition, as long as the

47   necessary illumination can be maintained over a larger surface in the sample plane.

48   Extending the array of patterned excitation has been used to increase the speed or FOV of

49   confocal[6], STED[7,8] and SIM imaging[9], but ensuring the quality of the extended pattern

50   across a larger FOV remains a limiting factor. For SMLM, flat-fielding approaches made it

51   possible to extend super-resolution imaging over ~100x100 μm^2 FOVs[10,11], but their transfer

52   to patterned illumination remains limited.

53   An entirely different approach to effectively achieve super-resolution modifies

54   sample preparation rather than image acquisition. By physically increasing the size of the

55   specimen in an isotropic manner via expansion microscopy[12] (ExM), overall imaging

56   throughput can be increased by opting for faster diffraction-limited microscopes[12–14].

57   Alternatively, combining ExM with existing super-resolution microscopies allows even

58   further improvement in resolution[14–18], since the resolvable scale is reduced by the

59   expansion factor. However, expansion exacerbates limitations in imaging throughput since

60   the effective FOV size is divided by the expansion factor along each dimension[19].

61   Therefore, fast, parallelized, super-resolution techniques with large FOVs present an

62   advantage for imaging ExM samples, among other applications.

63   The instant structured illumination microscope (iSIM)[9] uses parallelization in the

64   form of multifocal excitation and optical image processing to achieve a two-fold

65   improvement in resolution, at frame rates reaching 100 Hz. While this gives the iSIM good

66   potential for high-throughput super-resolution imaging, spatially varying illumination

67   produces a spatially dependent signal to noise ratio while restricting the imaging FOV to

68   ~50x50 μm^2. Although solutions for producing homogeneous multi-focal excitation exist

69   using diffractive optical elements[20], spatial light modulators (SLM)[21], multi-mode fibers[22] or

70   beam splitters[23], each suffers from some combination of a limited number of excitation

71   spots[20,21,23], heterogeneity[21,23] or low transmission efficiency[20].

72   In this work, we develop a flat-fielding element for multi-focal excitation, dubbed

73   mfFIFI. Our design is based on the Koehler integrator[24–26] and ensures that the

74   homogeneity, pitch and size of the excitation spots are optimized. We integrate mfFIFI into

75   an iSIM to engineer an instrument capable of 3D multi-color imaging with uniform quality

76   and doubled resolution over a 100x100 µm^2 FOV. We further parallelize the acquisition

77   across multiple FOVs, stitching them together to create seamless montages of tens of

78   super-resolved living cells within seconds, enabled by the homogeneous illumination.

79   Finally, we combine the mfFIFI iSIM with ultrastructure expansion microscopy (U-ExM)[31] to

80   perform high-throughput super-resolution imaging with an effective resolution of ~35 nm.

81   We use this to collect 3D images of hundreds of expanded centrioles in human cells, and

82   thousands of expanded purified *Chlamydomonas reinhardtii* centrioles. These particles are

83   averaged to reconstruct maps of post-translational modifications (PTMs) of centriolar

84   tubulin, revealing differences in the spatial organization of acetylation, monoglutamylation

85   and polyglutamylation.

86   **Results**

87   **Design and implementation of homogeneous multifocal excitation**

88   Generating a uniform irradiance over a large FOV while retaining the highest

89   achievable resolution requires the following properties of the excitation focal spots in a

90   multi-focal microscope: 1) homogeneous intensity, 2) constant pitch and 3) diffraction-

91   limited size across the field of view. Existing methods for generating uniform excitation are

92   often limited to producing a low number of excitation spots, with residual heterogeneity and

93   low transmission efficiency. Thus, we set out to extend the Koehler integrator[24–26], which

94   averages over the spatial and angular distributions of the light source to homogenize the

95   beam, for use with multifocal excitation.

96

4
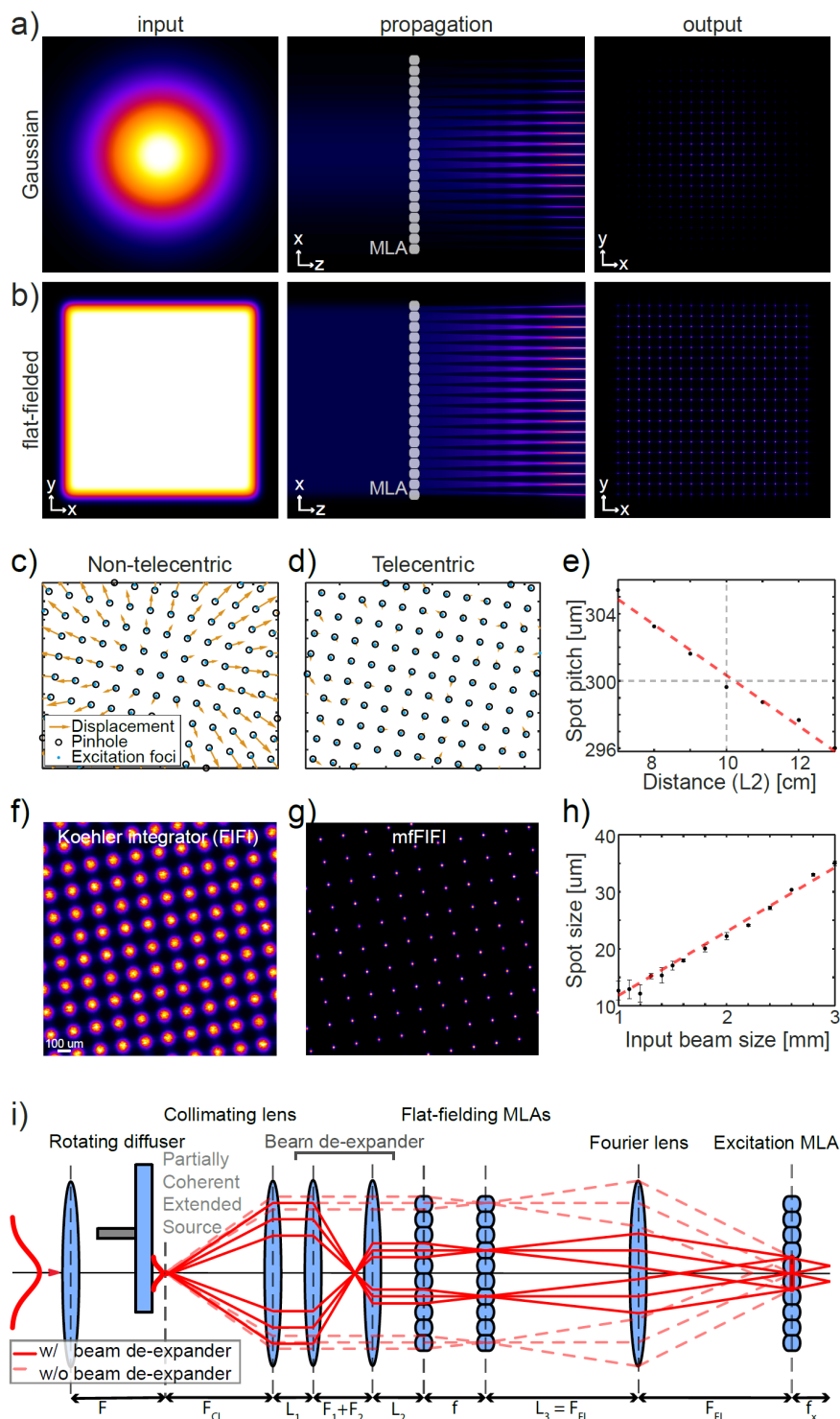
Figure 1 – Design and features of the mfFIFI module. a,b) Wave optics simulation with (a) a Gaussian beam or (b) a flat-top beam used as input onto the excitation MLA, showing their propagation and their effect on the output intensity of the generated excitation spots. c,d) Experimental positions of the excitation spots (blue dots) overlaid on a conjugate pinhole array (black circles) and the displacement between the two (yellow arrows) for (c)

104   non-telecentric and (d) telecentric illumination of the excitation MLA reveals a change in the

105   pitch of excitation spots caused by non-telecentric illumination. Data are from separately

106   acquired images of pinholes and excitation spots. e) Plot showing the dependence of the

107   pitch of the excitation spots on the offset of the Fourier lens back focal plane to the second

108   flat-fielding MLA. Dashed line represents zero offset on the x-axis and the ground truth set

109   by the pitch of the MLA on the y-axis. f) Image of excitation spots generated with a

110   Gaussian beam as input into the excitation MLA. Directly implementing the Koehler

111   integrator as the input results in large excitation spots. g) Limiting the number of flat-fielding

112   MLA channels used for beam homogenization partially recovers the size of the excitation

113   spots as achieved using Gaussian excitation (a), while maintaining uniform intensity of the

114   Koehler integrator (f). h) The spot size increases linearly with the diameter of the beam

115   incident on the flat-fielding MLAs over the given range. i) Complete design and

116   implementation of the extended Koehler integrator for multi-focal flat illumination for field

117   independent imaging (mfFIFI).

118   Previously, multifocal excitation for the iSIM was generated by illuminating a

119   microlens array (MLA) with a collimated Gaussian beam[6,9]. As expected, the non-

120   homogeneous beam profile results in excitation points whose intensity depends on their

121   location, a result which is recapitulated in a wave optics simulation (**Figure 1a**)

122   (**Supplemental information**). Alternatively, illuminating the excitation MLA with a flat-top

123   beam – such as that produced by a Koehler integrator – results in an array of multifocal

124   excitation spots of homogeneous intensity (**Figure 1b**). This can be achieved by placing the

125   excitation MLA at the front focal plane of the Fourier lens of the Koehler integrator, where

126   the flat-top is focused (**Supplemental Figure 1a**). However, if the incident wavefront is not

127   flat, the non-telecentric illumination of the excitation MLA produced by this configuration

128   alters the pitch of the excitation spots in the focal plane of the excitation MLA (**Figure 1c**).

129   This periodicity – usually determined by the pitch of the excitation MLA – must match the

130   periodicity of additional components that are typically placed in conjugate image planes of

131   confocal microscopes, such as a pinhole array. In the case of a mismatch of array

132   elements, the light will be gradually occluded and decrease in intensity away from the

133   center of the optical path. To solve this problem and achieve telecentric illumination of the

134   excitation MLA, we place the Fourier lens of the Koehler integrator one focal length away

6

135   from the second flat-fielding MLA[27], resulting in a flat wavefront and thereby ensuring that

136   the pitch of the excitation is conserved (**Figure 1d, Supplemental Figure 1b**). Additionally,

137   adjustment of the distance between the second flat-fielding MLA and the Fourier lens can

138   be used to finely adjust the resulting periodicity of the excitation spots to match that of the

139   other optical elements (**Figure 1e, Supplemental Figure 2a-d**). This feature, not shared by

140   refractive beam-shapers, allows us to optimize transmission efficiency.

141   Finally, in confocal microscopy and its variants such as iSIM, maximizing the

142   achievable resolution requires focusing the excitation light to a diffraction-limited spot on the

143   sample. This imposes a limitation on the spot size that should be generated in the excitation

144   path. However, implementing a traditional Koehler integrator in the excitation path would

145   produce large excitation spots due to the nature of the partially coherent extended source

146   created by the rotating diffuser (**Figure 1e-f, Supplemental Figure 1**). In that case, the

147   accessible improvement in resolution would not be based on diffraction-limited

148   performance. A possible solution would be to introduce a pinhole array to mask the

149   excitation spots that are focused onto the sample, but at a significant cost to the

150   transmission efficiency.

151   In an alternative design, we find that – contrary to the typical Koehler integrator

152   where illuminating a maximal number of flat-fielding microlenses is preferred[24–26] –

153   illuminating fewer microlenses offers a solution to control the excitation spot size and

154   ensure diffraction-limited excitation at the sample (**Figure 1g,h**). Incorporating a beam

155   expander to contract the light incident on the flat-fielding MLAs (referred to as a beam

156   contractor henceforth, **Figure 1i, Supplemental Figure 1c**) allows us to tune the apparent

157   size and angular distribution of the extended source. This shrinks the size of the excitation

158   spots, while maintaining efficient light transmission and homogeneity across the excitation

159   illumination. This configuration, which we call multifocal flat illumination for field-

160   independent imaging (mfFIFI), meets all the above requirements for homogeneous

161   multifocal excitation and is shown in **Figure 1i**.

162   These requirements can be described by geometrical optics and are a direct

163   outcome of ray transfer matrix calculations (**Supplemental information, Supplemental**

164   **Figure 2**), but the large parameter space makes the design and optimization of the mfFIFI

165   module non-trivial. For example, beam contraction presents a trade-off between

166   homogeneity of the multifocal excitation and the ability to achieve diffraction-limited

167   excitation and requires careful optimization (**Supplemental information, Supplemental**

168   **Figure 3h**). To facilitate the optimization and choice of components for efficient mfFIFI, we

169   provide the main design equations and an extended version of our existing wave optics

170   simulation platform[10] (**Supplemental information, Supplemental Figure 3, Supplemental**

171   **Table 1**).

172   **iSIM integration and performance characterization**

173   We tested the performance of the mfFIFI module when integrated into the excitation

174   path of an iSIM[14,31] (**Supplemental information, Supplemental Figure 4**). To visualize the

175   excitation illumination of the iSIM, we used a concentrated dye solution[28], and imaged the

176   emitted light onto the camera without scanning (**Supplemental information,**

177   **Supplemental Figure 4a**). Using an approximately Gaussian beam ($M^2 < 1.1$, FWHM

178   diameter ~12 mm) to create the excitation pattern, as used in the initial iSIM design[9,29],

179   results in excitation points of spatially varying intensity closely following a Gaussian

180   distribution (**Figure 2a**), as expected from the simulation (**Figure 1a**). Scanning the

181   Gaussian excitation points partially homogenizes the excitation along the scan direction;

182   however, the resulting illumination features a bright central region and strong roll-off away

183   from the central optical axis (**Supplemental information, Supplemental Figure 5a,b**). In

184   comparison, generating the excitation using the mfFIFI module results in a more uniform

185   multifocal excitation covering an area of approximately 100x100 μm^2 (**Figure 2b**), and a

186   more homogeneous excitation during scanning (**Supplemental information,**

187   **Supplemental Figure 5c-e**).

8
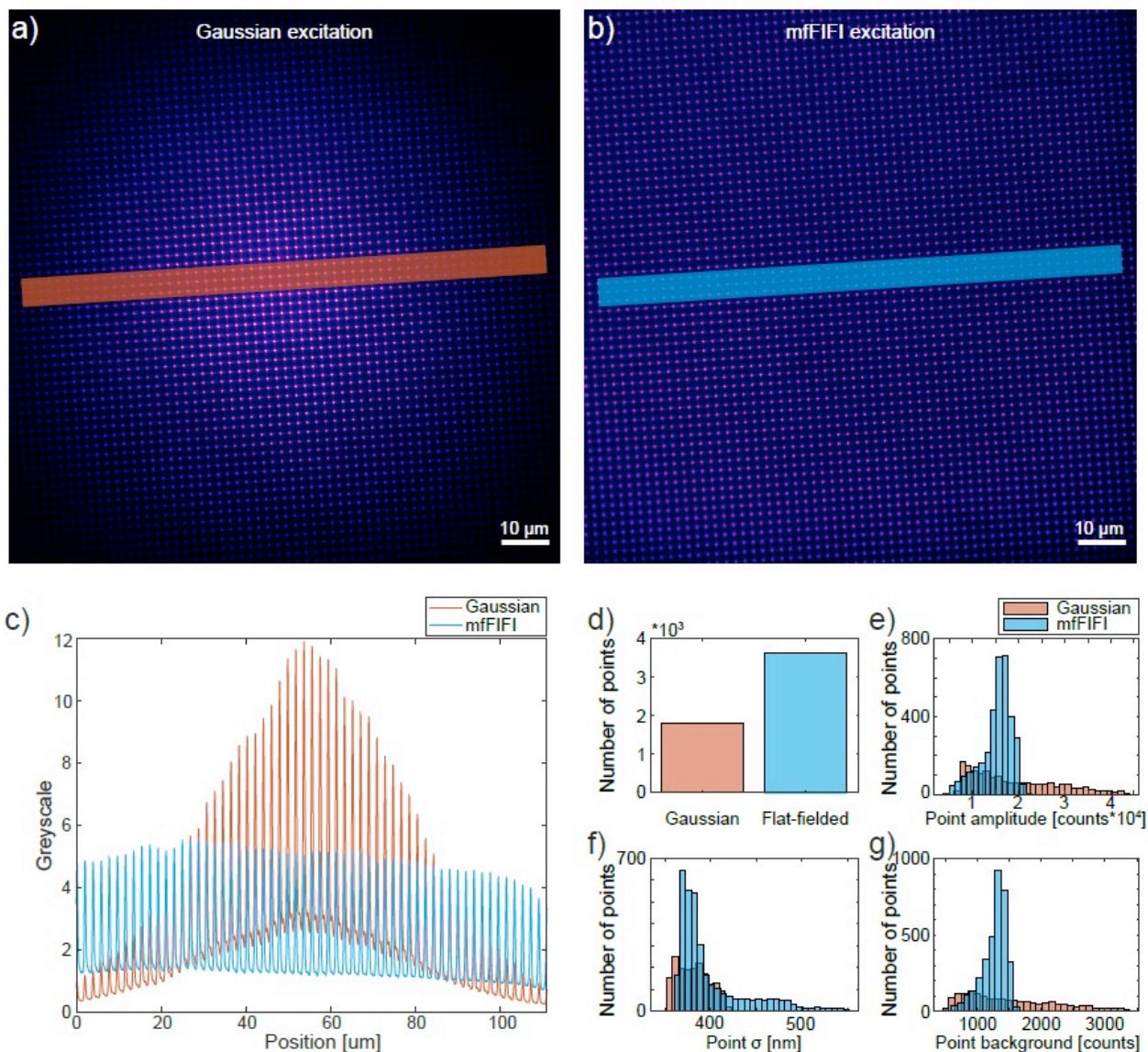
188

189 **Figure 2 – Performance comparison between Gaussian and mfFIFI excitation.** a,b)
190 Excitation points imaged onto a NaFITC fluorescent dye sample with (a) Gaussian and (b)
191 mfFIFI excitation. c) Intensity profiles measured along lines in (a, b). d) Number of
192 excitation points with a signal-to-noise ratio (SNR) above 3 in Gaussian and mfFIFI
193 excitation. mfFIFI increases the number of excitation points by a factor of two. e-g)
194 Histograms of excitation point (e) amplitudes, (f) variance and (g) background levels for
195 Gaussian and mfFIFI excitation.

196   Comparing intensity profiles along the rows of excitation spots shows that mfFIFI

197   efficiently redistributes the spatially varying input Gaussian excitation over a larger area

198   (**Figure 2c**). Quantifying these differences, we find that mfFIFI doubles the number of

199   excitation spots above background levels compared to the Gaussian excitation, while

200   resulting in a much narrower distribution of spot amplitudes and background (**Figure 2d-e,**

9

201 **g**). Furthermore, this improvement comes at no measurable cost to the quality of the

202 structured illumination. We find that both the size of the excitation spots required for

203 resolution improvement in confocal microscopy (**Figure 2f**) and their periodicity (222.3±0.3

204 μm (Gaussian) and 222.2±0.3 μm (mfFIFI) (mean ± S.D.)) are maintained, and compare

205 well with the ground truth (222 μm excitation MLA pitch) (**Supplemental information**). This

206 was further verified by imaging 100 nm fluorescent beads, showing comparable lateral

207 resolution between mfFIFI (214 ± 5 nm, mean ± S.D.) and Gaussian illumination (219 ± 12

208 nm), based on FWHM measured on raw iSIM data before deconvolution, or ~140 nm lateral

209 and ~350 nm axial resolution after deconvolution[9] (**Supplemental information**).

210 **Large FOV iSIM imaging and FOV stitching**

211 We used our custom-built iSIM setup as a platform to combine the capability of

212 mfFIFI excitation with a scientific complementary metal-oxide semiconductor (sCMOS)

213 camera for detection to perform large FOV volumetric imaging at doubled resolution. While

214 existing commercial SIM setups are mostly limited to FOVs with a linear dimension of 30-60

215 μm, our setup reaches >100x100 μm^2, thus providing a ~4- to 10-fold increase in FOV area.

216 We used mfFIFI iSIM to simultaneously image multiple mammalian cells within a single

217 FOV at doubled resolution (**Figure 3a, Supplemental Movie 1**). Accessible imaging

218 speeds are limited merely by the frame rate of the detector; thus, frame rates of up to 100

219 Hz as reported for iSIM[9,29] are preserved, since the increase in FOV is achieved by

220 improved parallelization from the increased number of illumination spots. Thus, the increase

221 in FOV translates directly into an increase in throughput.

222

223
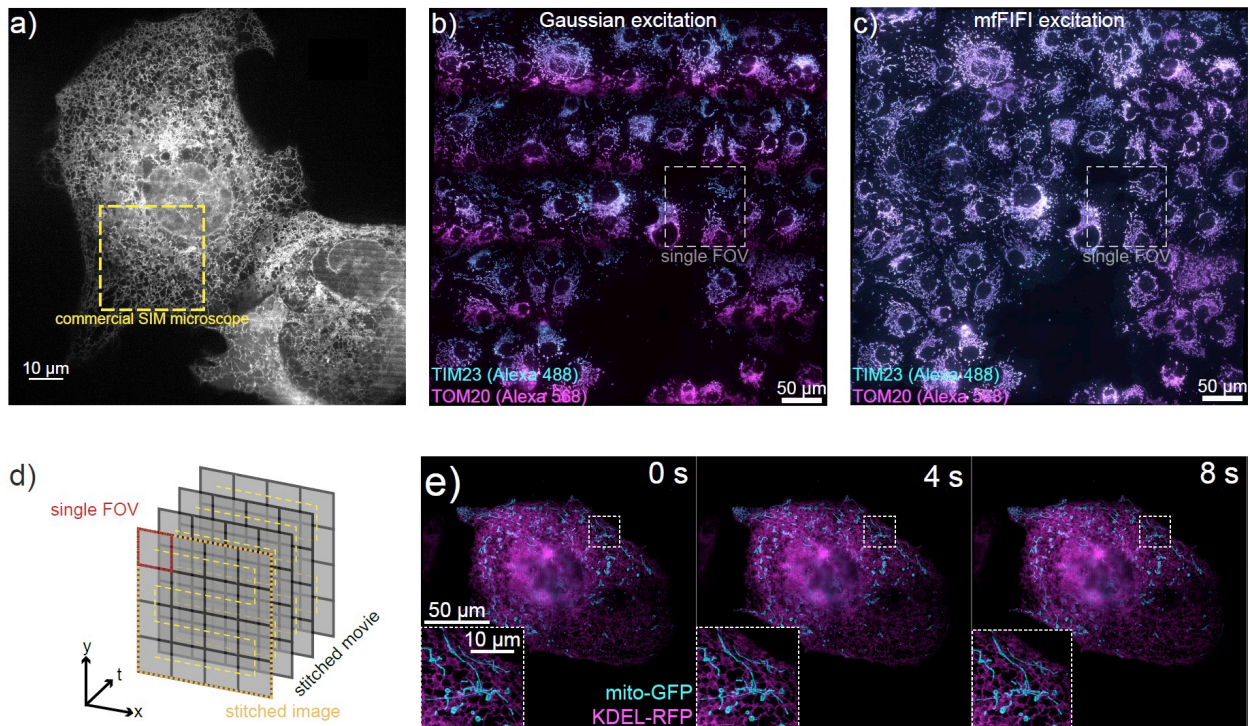
Figure 3 – Large FOV imaging and multi-FOV stitching. a) Cos7 cell expressing KDEL-RFP imaged with an iSIM using mfFIFI excitation and an sCMOS camera enabling imaging of FOVs up to ~115x115 µm^2 at doubled resolution compared to diffraction limited performance. Yellow square shows the size of a 30x30 µm^2 FOV available on a standard commercial SIM setup. Full movie shown in **Supplemental Movie 1**. b,c) Raw iSIM images of Cos7 cells immunolabelled for TIM23 and TOM20, stitched from a 5x5 grid of FOVs using (b) Gaussian and (c) mfFIFI excitation. d) Introducing an additional layer of parallelization into iSIM imaging by iterating over multiple FOVs allows trading off the speed of iSIM imaging to construct larger FOVs at high speed and doubled resolution compared to diffraction limited performance. e) Montage showing frames from a high-speed movie built up over a 2x2 grid of FOVs (**Supplemental information**, original movie 2s temporal resolution) of cells expressing mito-GFP and KDEL-RFP. Full movie shown in **Supplemental Movie 2**.

The effective image size can be further extended by stitching together adjacent FOVs. Such an approach requires homogeneous illumination to allow seamless stitching (**Figure 3b**). The speed of iSIM imaging combined with the large FOV enabled by mfFIFI allowed us to stitch together dual-color 3D stacks covering a 500x500x5 µm^3 volume with a 5x5 grid of FOVs, each acquired within 5 seconds. With this approach, within 2 minutes, we could capture 3D images of more than 80 cells stained for the mitochondrial inner (TIM23)

11

243   and outer (TOM20) membrane translocases, revealing coupled geometries of the two

244   membranes (**Figure 3b-c**). The current limiting factor for multi-FOV imaging is the speed of

245   stage translation and synchronization between stage translation and the rest of the iSIM

246   acquisition control (**Supplemental information**). In contrast, the same acquisition without

247   mfFIFI resulted in varying intensity across each FOV, with pronounced dark boundaries at

248   the borders of individual FOVs (**Figure 3b**).

249   For time-lapse imaging, we introduced an additional layer of parallelization by

250   iterating the acquisition procedure over a grid of FOVs (**Figure 3d**). By trading temporal

251   resolution for a gain in imaging area, we can use the speed of iSIM imaging to cover

252   multiple FOVs. For example, by iterating over a 2x2 grid of FOVs we could capture four

253   time more regions of close contact between mitochondria and ER, known to serve as

254   hotspots for mitochondrial division[30] at a temporal resolution of 2 seconds (**Figure 3e,**

255   **Supplemental Movie 2**) (**Supplemental information**). This illustrates how processes with

256   less demanding temporal dynamics can benefit from mfFIFI to extend the throughput of

257   iSIM without compromising spatial resolution.

258   **High-throughput super-resolution imaging of expanded centrioles**

259   A recently developed variant of ExM termed ultrastructure expansion microscopy

260   (U-ExM)[31] enables preservation of the structure and molecular identity of multi-protein

261   assemblies (particles). When combined with iSIM imaging, an expansion factor of ~4

262   results in an effective resolution of ~140 / 4 = 35 nm laterally and ~350 / 4 ≈ 90 nm axially

263   after deconvolution. Compared with current state-of-the-art super-resolution microscopes

264   with similar resolution performance, such as the HT-STORM[10] capable of imaging a

265   100x100 µm^2 FOV in ~5-10 minutes or a similar FOV with easySLM-STED[32] in 60-80

266   minutes, the iSIM is capable of stitching together images of expanded samples to form an

267   equivalent FOV within 2-5 seconds. This represents a 100-1000-fold improvement in

268   imaging throughput. Therefore, acquiring datasets of thousands of particles that would take

269   weeks or months to acquire on a conventional STORM or STED microscope require only 1-

270   2 hours on the high-throughput iSIM.

271   As a proof-of-concept for iSIM/U-ExM, we set out to analyze centrioles, organelles

272   found in most eukaryotic cells that seed the formation of the axoneme in cilia and the

273   centrosome in animal cells. Centrioles have a characteristic nine-fold radial symmetric

274   arrangement of microtubule triplets towards the proximal end of the organelle, composed of

275   complete A-microtubules and incomplete B- and C-tubules[33], with a transition to A- and B-

276   microtubule doublets towards the centriole distal end[34] (**Figure 4a**). It is known that

277   centriolar tubulin is enriched in post-translational modifications (PTMs), including

278   acetylation and polyglutamylation[35,36]. Acetylation is known to stabilize microtubules,

279   increase their flexibility and protect them against mechanical aging[37–39]. Glutamylation has

280   been postulated to likewise stabilize microtubules in the centriole and protect the organelle

281   from pulling and pushing forces acting during mitosis[36,40,41]. Although these observations

282   indicate that centrioles might be stabilized via tubulin acetylation and polyglutamylation, the

283   spatial organization of these PTMs on the organelle remains largely unexplored.

284   To analyze human centrioles in a similar stage of the cell cycle and of the centriole

285   duplication cycle, we synchronized RPE-1 cells with thymidine to arrest them at the G1/S

286   transition and with the Plk4 inhibitor Centrinone to prevent the formation of new centrioles[52].

287   After expansion and staining with antibodies against acetylated and polyglutamylated

288   tubulin, we imaged >100 centrioles in 3D in their cellular context per hour*,* revealing the

289   distribution of these PTMs along the organelle. Analyzing over 400 individual particles

290   extracted from these images (**Supplemental Figure 6**) revealed that centriolar tubulin

291   appears uniformly acetylated, while polyglutamylation terminates ~30 nm before the distal

292   end (**Figure 4b, Supplemental Figure 7a-c**). Moreover, the polyglutamylation signal

293   exhibits a larger diameter (**Figure 4b, Supplemental Figure 7a-c**), in line with the fact that

294   acetylation occurs witin the microtubule wall and polyglutamylation on the outer surface of

295   the polymer[31].
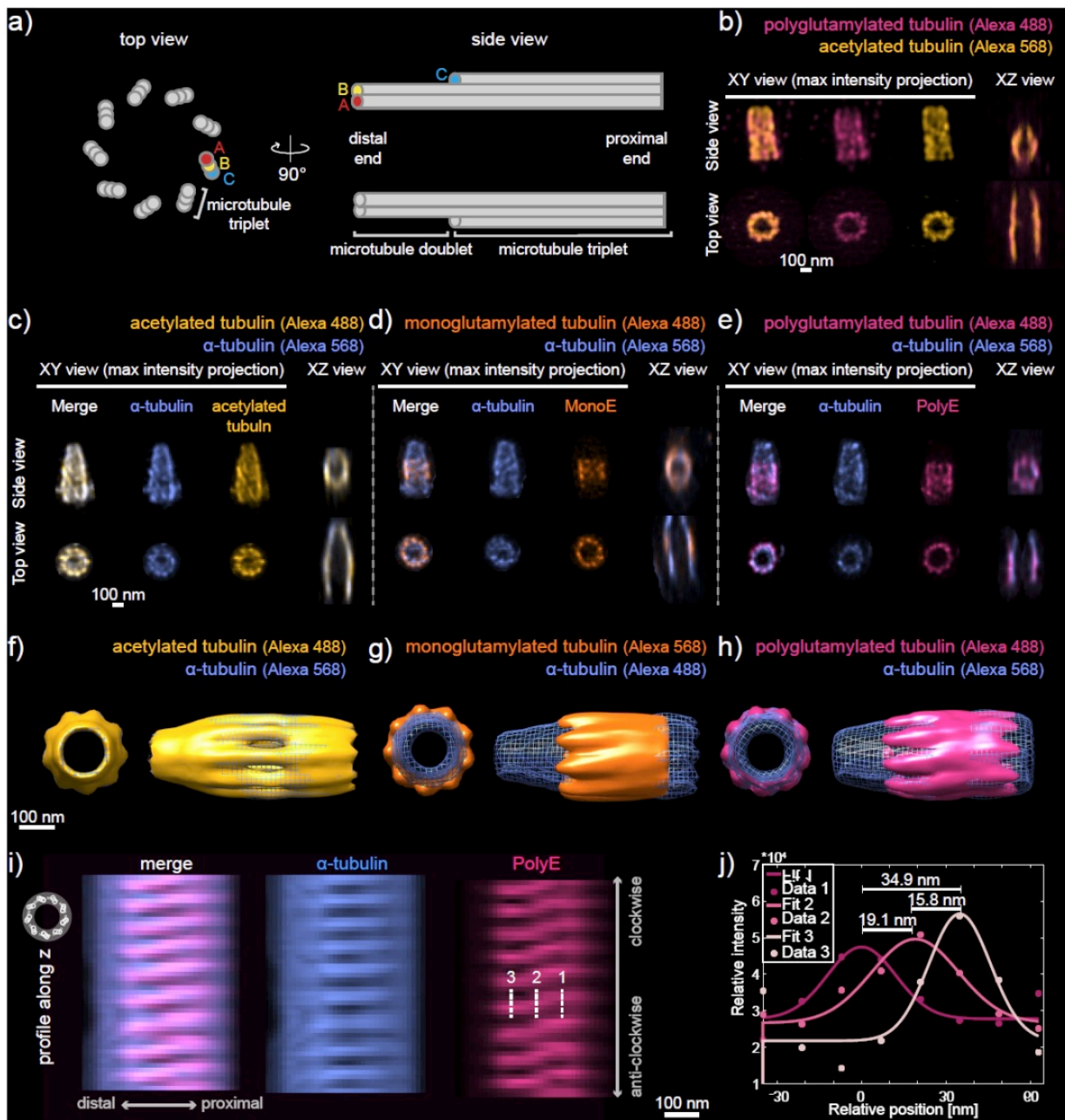
Figure 4 – High-throughput super-resolution imaging of expanded centrioles for mapping post-translational modifications of centriolar tubulin. a) Schematic representation of the centriolar microtubule wall viewed from the side (left) and top from the distal end. The A-, B- and C-microtubules are indicated. b) Examples of individual mature human centriole particles orthogonal (side view) or parallel (top view) to the optical axis collected in expanded RPE-1 cells labelled for acetylated tubulin and polyglutamylation (PolyE). The lateral (XY) maximum intensity projection and axial (XZ) cross sections are shown. c-e) Examples of individual purified *Chlamydomonas reinhardtii* centriole particles viewed orthogonal (side view) or parallel (top view) to the optical axis labelled for α-tubulin as reference and (c) acetylated tubulin, (d) monoglutamylated tubulin (GT335, MonoE) and (e) polyglutamylated tubulin (PolyE). f-h) High resolution particle averaging reconstructions

14

308   of (f) acetylated tubulin, (g) MonoE and (h) PolyE with α-tubulin as reference. Scale bars:

309   100 nm (pre-expansion). Top views shown from the distal end. i) Circular axial projection

310   (XZ profile) of the centriole reconstruction from (h) showing α-tubulin and PolyE signal

311   around the centriole (viewed from the outside). j) Intensity profiles measured along the

312   dashed lines from (i) showing the radial displacement of the PolyE signal.

313   To further increase throughput, we sought to expand purified centrioles to capture

314   dozens of pairs within a single FOV rather than just one per cell. We used centrioles

315   purified from *Chlamydomonas reinhardtii* to this end since the U-ExM protocol had been

316   optimized for this species[31]. Similarly to what we observed with human centrioles in the

317   cellular context, we observe that in centrioles purified from *Chlamydomonas reinhardtii*,

318   acetylated tubulin colocalizes with the microtubule wall along the entire length of the

319   organelle (**Figure 4c**), in agreement with previous reports[42]. In contrast, we found that

320   tubulin monoglutamylation (MonoE) is concentrated in the central core region of

321   *Chlamydomonas reinhardtii* centrioles (**Figure 4d**), as previously reported[42]. Since MonoE

322   recognizes the first glutamylation branching required for polyglutamylation (PolyE), we

323   would expect the distribution of PolyE to partially or completely overlap with that of MonoE.

324   Surprisingly, we found that although PolyE also localizes on the outer surface of the

325   microtubule triplets where it has been suggested to localize to the C-microtubule[31], it covers

326   a wider band along the length axis than MonoE (**Figure 4e, Supplemental Figure 7, 12**).

327   This difference could reflect lower MonoE antibody labelling efficiency, since saturating the

328   signal shows similar MonoE/PolyE localization.

329   The high throughput offered by mfFIFI-iSIM allowed us to collect 3D images of

330   thousands of purified expanded *Chlamydomonas reinhardtii* centrioles per hour

331   (**Supplemental Figure 8**, **Supplemental Table 2**). Having obtained 3D rather than 2D

332   particles allowed us to use fewer particles to perform averaging and high-resolution

333   multicolor reconstruction[44] compared to previous approaches using STORM[45] or electron

334   microscopy[46,47]. Thus, we classified particles before reconstruction to identify and average

335   only those particles sharing a high degree of similarity (ranging from 10-50% of the whole

336   dataset), and thereby achieve even higher resolution reconstructions (**Figure 4f-h**,

337 **Supplemental information, Supplemental Figure 9**). Here, we have focused on the most

338 frequently appearing class, but other classes could also be independently reconstructed.

339 For mapping multiple PTMs within the centriole, we employ dual-color labeling, using α-

340 tubulin staining of the microtubule triplet wall as a reference to subsequently align all PTMs

341 (**Supplemental Figure 10**).

342 The resulting reconstructions revealed an unexpected shift in the tangential position

343 of the PolyE signal from the proximal to the distal end (**Figure 4h**), which is also sometimes

344 visible in individual raw particles (**Supplemental Figure 8b inset, Figure 4e**). To account

345 for this shift, we considered two possibilities: 1) the whole microtubule triplet twists around

346 its axis while the PolyE signal remains localized to the C-microtubule[48] giving it an apparent

347 twist, and 2) the PolyE signal changes microtubule localization within the microtubule triplet.

348 Arguing against the first possibility, the microtubule triplet twists only within ~100 nm of the

349 proximal end (Le Guennec et al., in press), while in our reconstruction the PTM twist occurs

350 within a wider region covering ~250 nm from the proximal end,. Moreover, we determined

351 that the first possibility would be expected to cause a moderate ~6 nm shift of the PolyE

352 signal, and the second a more pronounced ~35-40 nm shift (**Supplemental information**,

353 **Supplemental Figure 11**). From our reconstruction, we measure a twist of ~34.9 nm,

354 which cannot be explained purely by twisting of the microtubule triplet (**Figure 4i,j**,

355 **Supplemental information, Supplemental Figure 11**). Therefore, we propose that

356 polyglutamylation changes localization within the microtubule triplet along the centriole,

357 moving from A- on the proximal end to the C-microtubule more distally.

358 **Conclusion**

359 To summarize, we designed a flat-fielding method for efficient multifocal excitation,

360 accompanied by a wave optics simulator which ensures optimal resolution performance.

361 While the Koehler integrator has spot generating properties when used with coherent

362 illumination, it introduces a strong wavelength dependence of the periodicity, making it

363 unsuitable as such for multi-color applications[26]. mfFIFI provides a largely wavelength-

16

364 independent solution for generating homogeneous multi-focal excitation, while benefiting

365 from the homogenizing properties of the Koehler integrator. We implemented the mfFIFI

366 module into an iSIM microscope, since its fast acquisition speeds and resolution doubling

367 give it good potential for high-throughput super-resolution imaging. However, the mfFIFI

368 module could be extended to any multi-focal excitation microscope such as a spinning disk

369 confocal microscope[6] using a Nipkow disk configuration, but not with other flat-fielding

370 solutions using diffractive optical elements[20], spatial light modulators (SLM)[21] or beam

371 splitters[23]. Furthermore, combining mfFIFI with phase masks required for donut beam

372 shaping could extend its application to parallelized STED and RESOLFT microscopes.

373 Flat-fielding enables multi-field of view imaging, which is a powerful way to maintain

374 resolution while increasing the effective image size to span more length scales. This is

375 important for sample spanning multiple fields of view, as in the case of tissues, or expanded

376 samples. ExM sacrifices the effective FOV to increase resolution, and stitching provides a

377 way to maintain throughput, allowing cellular features or structures to be imaged *in situ*, as

378 we demonstrate by imaging hundreds of human centrioles in cells.

379 Particle averaging and reconstruction is traditionally used in ultrastructural biology,

380 and leverages large datasets to capture the intrinsic variability within particles through

381 classification before reconstruction, while averaging out the noise. In the case of ExM,

382 different gels can have slightly different expansion factors, but this issue is circumvented by

383 our iSIM setup since thousands of particles can be acquired from a single gel section (~5x5

384 mm^2). In our case, the collected datasets were sufficiently large to allow particle

385 classification prior to averaging, an approach which improves the resolution of the

386 reconstruction and which, to our knowledge, has not been previously used for fluorescence

387 super-resolution. In addition to a 100-1000-fold improvement in throughput of iSIM/U-ExM

388 over HT-STORM[10,45] or easySLM-STED[32], expanded samples offer enhanced accessibility

389 of antibodies to bind proteins in crowded assemblies. Beyond particle averaging, high-

390 content or machine learning approaches rely on large datasets for training or screening,

391 and can benefit from the combination of throughput and resolution described here.

17

392   Our previous attempts to image centriolar microtubules with STORM proved largely

393   unsuccessful, restricting previous studies to the more accessible epitopes[45]. Here, we

394   reveal previously unobserved molecular organization, showing high coverage of

395   polyglutamylation in human centrioles, as well as precise localization to microtubule triplets

396   along the *Chlamydomonas reinhardtii* centriole. We find that polyglutamylation appears to

397   shift from the A-microtubule proximally to the C-microtubule more distally. It is possible that

398   such a glutamylation shift reflects a centriolar tubule code that defines the spatial

399   boundaries of the various elements that compose it, which could determine the positioning

400   of different structural elements along the length of the organelle.

401

402   **Methods**

403   **Sample preparation**

404   Cos-7 and RPE-1 cells were grown in Dulbecco's modified Eagle medium (DMEM)

405   supplemented with 10% fetal bovine serum (FBS). Cells were plated on 25 mm, #1.5 glass

406   coverslips (Menzel) 16-24 h prior to transfection or fixation at a confluency of ~10^5 cells per

407   well.

408   Transfections using [insert], were performed with Lipofectamine 2000 (Life

409   Technologies) using 150 ng of [insert] and 1.5 µL of the Lipofectamine 2000 reagent in 100

410   µL Opti-MEM medium per 6 well.

411   For synchronization of RPE-1 cells at the G1/S transition and the onset of centriole

412   assembly, ~125'000 cells were seeded for 24 h in six well-plates (Merck, TPP, 92006) on

413   12 mm coverslips in DMEM [insert]. Thymidine (Merck, T1895, 1 mM) and Centrinone

414   (Lucerna-Chem, MCE-HY-18682, 300 nM) were added for 18 h, before fixation of cells with

415   -20°C methanol for 5'.

416   For immunofluorescence experiments with COS-7 cells, cells were washed in pre-

417   warmed PBS before being fixed in pre-warmed fixation buffer (4% paraformaldehyde in

418   PBS). Cells were then permeabilized in 0.25 % Triton-X in PBS for 10 min. After washing in

419   PBS for 5 min, cells were incubated in blocking buffer (1% BSA in PBS) for 60 min. The

420   primary antibodies (Tom20-rabbit (1:50, FL-145 sc-11415 Santa Cruz Biotechnologies),

421   Tim23-mouse (1:100, 611222 BD Biosciences)) diluted in blocking buffer were incubated

422   for 60 min before washing 3 times in 0.2% BSA with 0.25% Triton-X in PBS for 10 min.

423   Secondary antibodies (AlexaFluor 488 goat anti-mouse IgG (H+L) (1:150, A28175

424   ThermoFisher), AlexaFluor 568 goat anti-rabbit IgG (H+L) (1:150, A11011 ThermoFisher))

425   were diluted in blocking buffer before incubation for another 30 min. The sample was

426   incubated in the dark, then washed 3 times with PBS before imaging.

427 **iSIM imaging**

428   The iSIM setup was partly based on previously described implementations[9,29]. Two

429 lasers with wavelengths of 488 nm (Sapphire 488-300 CW CDRH, Coherent) and 561 nm

430 (gem 561, Laser Quantum GmbH) were combined using a dichroic mirror (F48-486,

431 Analysentechnik) and controlled through an acousto-optic tunable filter (AOTFnC-400.650-

432 TN, AA Optoelectronic). In the case of Gaussian excitation, the beam was expanded with a

433 10x beam expander (f_{1a} = 40 mm, f_{2a} = 400 mm, Thorlabs). In the mfFIFI path, a focusing

434 lens (f_{FC} = 50 mm) was used to focus the light near a rotating diffuser (2.5° ± 0.25° FWHM

435 at 650 nm, 24-00066, Süss MicroOptics SA) before collimation by a collimating lens (f_{CL} =

436 60 mm, Thorlabs). The collimated beam was contracted by a factor of 4 by two lenses (f_{1b} =

437 120 mm, f_{2b} = 30 mm, Thorlabs) before illuminating two flat-fielding MLAs (300 μm pitch,

438 10mm x 10 mm, f = 4.78 mm, square lenses, 18-00157, Süss MicroOptics SA). The flat

439 field was then focused by a Fourier lens (f_{FL} = 300 mm, Thorlabs). Both paths then

440 illuminated the excitation MLA (222 μm pitch, 1" diameter, f = 6 mm, square lenses APO-Q-

441 P222-R2.74, Advanced Microoptic Systems GmbH). The excitation was relayed by scan

442 lenses (f_{SL} = 190 mm, 55-S190-60-VIS, Special Optics) to and from the scanning mirror

443 (SPO9086 Rev B Coated X Mirror, Sierra Precision Optics) mounted on a galvanometer

444 scanner (QS-12, N-2071, Nutfield Technology). The excitation was then imaged onto the

445 sample using a tube lens (f_{TL} = 350 mm, 49-289-INK, Edmund Optics) and an objective lens

446 (APON60XOTIRF, Olympus), resulting in a final magnification of ~116x. The sample was

447 placed on a precision aligned microscopy platform including a micropositioning control

448 (RM21-AZ-AXY-RMS-M, Mad City Labs) and a Z piezo stage (Nano-Z200, Mad City Labs).

449 The emission was relayed back through the excitation side of the scanning mirror and split

450 using a dichroic mirror (F58-488S, Semrock). The emission was then pinholed with a

451 pinhole array (chrome on 0.090-inch-thick quartz, 222 μm pitch, 40 μm diameter,

452 Photosciences) and relayed by two relay lenses (f_R = 300 mm, Thorlabs) before contracting

453 each emission spot by a factor of 2 using another MLA (222 μm pitch, 1" diameter, f = 0.93

454   mm, square lenses APO-Q-P222-R0.425, Advanced Microoptic Systems GmbH). The

455   emission was then relayed using scan lenses on the emission side of the scan mirror,

456   towards a filter wheel (Lambda 10-B, Sutter Instruments, Science Products) with 2 notch

457   filters (NF-03-488E-25 and NF-03-561E-25, Semrock) mounted to block the excitation

458   wavelengths. The transmitted emission was then collected by a sCMOS camera (PrimeBSI,

459   01-PRIME-BSI-R-M-16-C, Photometrics). The size of a square camera pixel corresponds to

460   56 nm on the sample.

461   The microscope was controlled using a custom written MATLAB script which

462   controlled an analog output card (PCI-6733, National Instruments) and breakout box (BNC-

463   2110, National Instruments) for precise control and synchronization of the scan mirror,

464   AOTF, camera and Z-stage. The XY stage and camera were controlled through

465   MicroManager[49].

466   For live cell imaging, imaging was performed at 37 °C in pre-warmed Leibovitz

467   medium in a top stage incubator (H301-PRIOR-NZ100-H117, Okolab). Imaging of

468   immunostained samples was performed in PBS. Expanded samples were mounted as

469   previously described[31]. Briefly, the expansion factor was determined before imaging by

470   measuring the gel size with a caliper (precision ±0.01 mm). The gel was then cut using a

471   razor, before removing excess water and placing the gel on a poly-D-lysine treated

472   coverslip (25 mm round coverslips, Mendel #1.5) already placed inside the imaging

473   chamber. After gently pressing on the gel to ensure attachment to the coverslip, a few

474   drops of ddH$_2$O were added on top of the sample to avoid shrinkage during imaging.

475   Image acquisition was performed using a custom written MATLAB script, in combination

476   with MicroManager[49].

477   **iSIM deconvolution**

478   Raw iSIM images were deconvolved using the Lucy-Richardson deconvolution

479   algorithm implemented in MATLAB and provided by Dr. Hari Shroff[9]. Each raw z-stack was

480   deconvolved for 40 iterations.

481 **mfFIFI characterization platform**

482   An optical characterization setup was built to measure the variation in pitch and spot

483 size of the multifocal points. A laser beam with a wavelength of 640 nm (CUBE 640-100C,

484 Coherent) was expanded with a 6x beam expander (f = 50 mm, f = 300 mm, Thorlabs) with

485 a pinhole (P50D, Thorlabs) at the joint focal plane of the two lenses to spatially filter the

486 beam. The beam is passed through a Köhler integrator, made of the following components:

487 focusing lens (f = 80 mm, Thorlabs), rotating diffuser (2.5° ± 0.25° FWHM at 650 nm, 24-

488 00066, Süss MicroOptics SA), collimating lens (f = 40 mm, Thorlabs), two flat-fielding MLAs

489 (300 μm pitch, 10mm x 10 mm, f = 4.78 mm, square lenses, 18-00157, Süss MicroOptics

490 SA), Fourier lens (f_{FL} = 300 mm, Thorlabs). An iris (ID25, Thorlabs) is used before the two

491 MLAs to control the portion of the beam which is allowed to propagate forward to reach and

492 illuminate MLAs, by adjusting the opening diameter of the iris. An excitation MLA (300 μm

493 pitch, 10mm x 10 mm, f = 8.72 mm, square lenses, 18-00221, Süss MicroOptics SA) is

494 used to produce the multifocal points. The size of the multifocal illumination is reduced by a

495 factor of 0.6x by a beam de-expander (f = 50 mm, f = 30 mm, Thorlabs) to be of appropriate

496 size for the sensor of the camera (DCC1545M, Thorlabs).

497   To obtain the data shown in Figure 1e, h, we used the characterization platform to

498 test the parameters affecting the spot size and pitch. A Vernier caliper was used to

499 measure the iris opening diameter, which was varied methodically to control the size of the

500 beam which illuminates the MLAs. Images of the beam at different iris opening diameters

501 were analyzed using a MATLAB script, which allowed us to fit each excitation point to a 2D

502 Gaussian and measure the multifocal points' mean spot FWHM as function of iris diameter.

503 In order to study the variation in the pitch of the multifocal points, the distance between the

504 Fourier lens and the second flat-fielding MLA was varied by displacing the flat-fielding

505 MLAs. A MATLAB script is used to measure the mean pitch at each distance, so that the

506 relationship between this distance and the pitch can be determined.

22

507   **Image analysis**

508   **Plateau uniformity quantification**

509   The homogeneity was quantified using the plateau uniformity definition based on the

510   FWHM of the histogram of the intensity values, according to ISO, ISO 13694:2018: Optics

511   and optical instruments - lasers and laser-related equipment - test methods for laser beam

512   power (energy) density distribution.

513   **Illumination profile measurement**

514   The illumination profiles used to optimize the pitch (telecentricity) and spot size of

515   the multifocal excitation were visualized using a small color CMOS camera (DCC1645C,

516   Thorlabs), placed in an intermediate image plane of the iSIM, between the second scan

517   lens and tube lens, to avoid introducing other aberrations along the whole optical path of

518   the iSIM.

519   The excitation profile at the sample was measured using a highly concentrated

520   fluorescent dye sample[32], as previously described[9]. Briefly, sodium fluorescein (NaFITC)

521   powder was diluted in deionized water, followed by vortexing and sonication until the

522   powder was completely dissolved. A 10 µL drop was placed on a 25 mm coverslip, before

523   covering with a 12 mm coverslip. The sample was then sealed using nail polish. The same

524   dye sample was used to measure both the 488 nm and 561 nm illumination profiles. The

525   illumination spots were characterized by fitting a 2D Gaussian to the intensity image. The

526   threshold was set so that no points in the background were detected. The scanning profiles

527   were measured with a 150 pixel thick line in Fiji[50].

528   In the case of excitation spots visualized in Figure 1f, g and the quantification in

529   Figure 1e, h, the illumination profile was imaged directly onto a camera placed in a

530   conjugate image plane.

531

Bead FWHM analysis

533   To characterize the performance of the iSIM microscope, we used 100 nm

534   Tetraspeck beads (ThermoFisher Scientific, T7279) deposited on poly-L-lysine treated

535   coverslips. Bead size was determined by fitting a Gaussian profile to the intensity profile of

536   the bead and extracting the FWHM.

537

Centriole shape and coverage analysis

539   To analyze the diameters of different PTM localizations within the centrioles, we

540   measured the intensity profile through the centers of top view centrioles (central plane,

541   centriole barrel parallel to the imaging axis). The profile was measured using a 7 pixel thick

542   line in Fiji[50]. Each peak was fitted to a Gaussian profile to localize its center, before

543   calculating the diameter as the distance between the two peaks on opposing sides of the

544   centriole ring.

545   To analyze the PTM distribution along the length of the centriole and their coverage,

546   we measured the intensity profile along the length of the centriole using a 10 pixel thick line

547   and from summed intensity projections of side view centrioles (centriole barrel orthogonal to

548   the imaging axis). We then took the width of the profile at ¼ of the maximal signal as the

549   length, to be less susceptible to noise. The coverage was then calculated by dividing the

550   length of the PTM in question, by the length of the reference label (acetylated tubulin for

551   human centrioles and α-tubulin in the case of *Chlamydomonas reinhardtii* centrioles).

Multiple field of view stitching

553   For stitching of multiple images, raw images or z-stacks were acquired with a 10%

554   overlap for both Gaussian and mfFIFI excitation. The acquired images were then combined

555   using the Grid/Collection stitching tool in Fiji[50] using the linear blending method with the

556   default values of 0.30 for regression threshold, 2.50 for max/avg displacement threshold

557   and 3.50 for absolute displacement threshold.

558   **Wave optics simulations**

559   The mfFIFI simulation platform has been adapted based on previous work[9]. All

560   simulations are based on standard numerical Fourier optics algorithms and rely on angular

561   spectrum propagation methods to simulate the propagation of an optical wave. An initial

562   simulation showing the effect of illuminating the excitation MLA with Gaussian and flat-

563   fielded profiles was performed using phase masks to represent optical components.

564   The parameters used for the simulation are summarized in **Supplemental Table 1**.

565   **Centriole expansion protocol**

566   *Chlamydomonas reinhardtii* centrioles were isolated from the cell-wall-less strain

567   CW15-[51] and expanded using the U-ExM protocol[31]. Briefly, isolated centrioles were spun

568   on 12mm Poly-D-Lysine-coated (ThermoFisher, A3890401) coverslips prior to U-ExM. For

569   human cell expansion, cells were initially seeded on 12 mm coverslips before being fixed

570   with 4% PFA. Coverslips were then incubated in a solution of 0.7% formaldehyde and 1%

571   acrylamide in PBS for 4-5 hours at 37˚C. Next, coverslips were incubated in the monomer

572   solution for 1 minute on ice and then shifted to 37˚C, for 1 hour in a dark and humidified

573   chamber. For one gel, the monomer solution is made of 25 µL sodium acrylate (Sigma-

574   Aldrich, 408220, 38% (wt/wt, diluted with nuclease-free water)), 12.5 µL acrylamide (Sigma-

575   Aldrich, A4058, 40% stock solution), 2.5 µL N,N'-methylenbisacrylamide (Sigma-Aldrich,

576   M1533, 2% stock solution), and 5 µL 10X PBS, supplemented with 2.5 µL TEMED and 2.5

577   µL APS (from 10% stock solutions). Once polymerized, gels were moved into denaturation

578   buffer (200 mM SDS, 200 mM NaCl and 50 mM Tris in nuclease-free water, pH 9) for 15

579   minutes at room temperature with gentle shaking and then shifted for 30 minutes to 95˚C in

580   an 1.5 mL Eppendorf tube with 1 mL of fresh denaturation buffer. Then, gels were placed at

581 room temperature in beakers with 200 mL of distilled water. Water was exchanged twice

582 (every 30 min) and the sample was incubated overnight at room temperature. The following

583 day, water was changed with PBS for 15 min at room temperature. Gels were then

584 incubated for 3h at 37°C with gentle shaking in 1 mL of primary antibody solution (in 3%

585 BSA and 0.05% Tween20). Samples were then washed three times for 10 min with PBS

586 supplemented by 0.1% Tween20 while shaking, followed by incubation with secondary

587 antibodies for 3h at 37°C in 3% BSA and 0.05% Tween20. Finally gels were washed 3x in

588 T-PBS. For RPE-1 cells, the sample was supplemented in the second wash with Hoechst

589 33258 (1:2'000) dye and place in beakers with 200 mL of distilled water for final expansion,

590 with again water being exchanged twice for 30'. Before imaging, gels were again expanded

591 overnight in ddH$_2$0. Primary antibodies used to image centrioles in expanded RPE-1 cells

592 were rabbit anti-polyglutamate chain (polyE), pAb (IN105, 1:250) and mouse monoclonal

593 anti-acetylated tubulin (Merck, T7451, 1:500). Secondary antibodies were goat anti-Rabbit

594 Alexa488 (Thermo-Fisher Scientific, A11034, 1:500) and goat anti-mouse IgG Alexa 568

595 F(ab')2 (Thermo-Fisher Scientific, A11019, 1:500).The following primary antibodies were

596 used for imaging expanded purified *Chlamydomonas reinhardtii* centrioles: rabbit polyclonal

597 anti-polyglutamate chain (PolyE, IN105,1:500, AG-25B-0030-C050, Adipogen), mouse

598 monoclonal anti-α-tubulin (DM1α,1:500, T6199, Sigma-Aldrich), mouse monoclonal anti-

599 polyglutamylation modification (GT335,1:200, AG-20B-0020, Adipogen), mouse monoclonal

600 anti-acetyl-α-tubulin   (Lys40,1:50, 32-2700, Invitrogen, ThermoFisher). Secondary

601 antibodies were goat anti-rabbit Alexa Fluor 488 IgG H+L (1:400, A11008), goat anti-mouse

602 Alexa Fluor 488 IgG H+L (1:400, A11029), goat anti-rabbit Alexa Fluor 568 IgG H+L (1:400,

603 A11036), goat anti-mouse Alexa Fluor 568 IgG H+L (1:400, A11004 all from Invitrogen,

604 ThermoFisher).

605 **Particle segmentation, classification and 3D reconstruction of purified centrioles**

606   Particles were segmented using a custom written Matlab script. Briefly, the

607 threshold value was found on the maximum intensity projections of the 3D stacks, before

26

608   applying it back to the individual stacks. The regions were then binarized and segmented

609   by connecting neighboring pixels across the 3D stack. The binarized points of interested

610   were then dilated to form the mask which was then applied back to the raw stack. The

611   particles were then cut out from the original stack with their specific mask and a 60x60 pixel

612   surrounding region. The segmentation was ~50% successful, mostly because centrioles are

613   often found in pairs, and closely located pairs had to be rejected since they could not be

614   segmented correctly.

615   After particles were segmented and up-sampled (to reach isotropic pixel size), the

616   particles with tubulin signal were aligned to a reference using Dynamo. The reference was

617   built using a reconstructed tubulin signal made from 12 manually selected particles. Once

618   particles were all similarly aligned, a cross-correlation matrix was generated by calculating

619   the similarity between each pairs of particles. The cross-correlation matrix was converted to

620   a distance matrix by subtracting cross-correlation values to 1. A hierarchical classification

621   was made using the Ward method (hclust function from R). The classification tree was

622   empirically cut into 10 groups. For each group, the average particle was generated for the

623   tubulin signal and for the PolyE signal by applying the transformation parameters obtained

624   during the alignment step. The 10 averages were compared to identify which groups were

625   most promising. The best classes were used to produce the reconstruction results of Figure

626   4. The reconstruction method was based on ref.[44], and followed the procedure reported in

627   ref.[31] with a C9 symmetry constraint. The point spread function was experimentally

628   measured by imaging 100 nm fluorescent beads (TetraSpeck™ Microspheres, 0.1 μm,

629   T7279 ThermoFisher). We made two modifications to the *reference-free* step of the

630   reconstruction algorithm[44]. Firstly, we adopted a multiscale reconstruction approach: we

631   used results obtained with coarsely subsampled data to get a coarse initialization. Thanks

632   to this approach, we were able to perform the reconstruction at the highest resolution in

633   reasonable computation time. Secondly, we decoupled the angular search of the

634   orientations: the first two Euler angles were estimated first, before the third one. This further

635   accelerated the reconstruction and provided sharper results in the case of C9 symmetry.

636   Reconstructions were visualized using Chimera, by setting the threshold to fit the

637   average length of the particles. Artefactual signals in the center of the reconstruction that

638   arise due to the imposed 9-fold symmetry were removed during post-processing.

Author contributions

650   D.M., K.M.D., P.Gö., V.H., P.Gu. and S.M. conceived and designed the project.

651   P.Gö., V.H., P.Gu and S.M. supervised the project. D.M., K.M.D. and S.M. designed the

652   multi-focal illumination system. D.M. and K.M.D. developed the simulation platform. D.M.

653   built the microscope, performed all experiments and data analysis. D.G. performed the

654   purified *Chlamydomonas reinhardtii* centriole sample preparation. D.F. performed single

655   particle averaging and reconstruction. N.B. performed the human RPE-1 centriole sample

656   preparation. M.L.G. performed the particle classification and alignment. K.I. built and

657   performed experiments on the flat-fielding characterization platform. D.M. and S.M. wrote

658   the manuscript with contributions from all authors.

659   **Competing interests**

660   The authors declare no competing financial interests.

661   **References**

662   1.   Rust, M. J., Bates, M. & Zhuang, X. Sub-diffraction-limit imaging by stochastic

663   optical reconstruction microscopy (STORM). *Nat. Methods* **3**, 793–796 (2006).

664   2.   Betzig, E. *et al.* Imaging Intracellular Fluorescent Proteins at Nanometer Resolution.

665   *Science (80-.).* **313**, 1642–1645 (2006).

666   3.   Gustafsson, M. G. L. Surpassing the lateral resolution limit by a factor of two using

667   structured illumination microscopy. *J. Microsc.* **198**, 82–87 (2000).

668   4.   Gustafsson, M. G. L. *et al.* Three-Dimensional Resolution Doubling in Wide-Field

669   Fluorescence Microscopy by Structured Illumination. *Biophys. J.* **94**, 4957–4970 (2008).

670   5.   Hell Stefan, W. & Jan, W. Breaking the diffraction resolution limit by stimulated

671   emission: stimulated-emission-depletion fluorescence microscopy. *Opt. Lett* **19**, 780–2

672   (1994).

673   6.   Tanaami, T. *et al.* High-speed 1-frame/ms scanning confocal microscope with a

674   microlens and Nipkow disks. *Appl. Opt.* **41**, 4704 (2002).

675   7.   Bingen, P., Reuss, M., Engelhardt, J. & Hell, S. W. Parallelized STED fluorescence

676   nanoscopy. *Opt. Express* **19**, 23716 (2011).

677   8.   Chmyrov, A. *et al.* Nanoscopy with more than 100,000 'doughnuts'. *Nat. Methods*

678   **10**, 737–740 (2013).

679   9.   York, A. G. *et al.* Instant super-resolution imaging in live cells and embryos via

680   analog image processing. *Nat. Methods* **10**, 1122–1126 (2013).

681   10.   Douglass, K. M., Sieben, C., Archetti, A., Lambert, A. & Manley, S. Super-resolution

682   imaging of multiple cells by optimized flat-field epi-illumination. *Nat. Photonics* **10**, 705–708

683   (2016).

684   11.   Archetti, A. *et al.* Waveguide-PAINT offers an open platform for large field-of-view

685   super-resolution imaging. *Nat. Commun.* **10**, 1267 (2019).

686   12.   Chen, F., Tillberg, P. W. & Boyden, E. S. Expansion microscopy. *Science (80-.).*

687   **347**, 543–548 (2015).

688   13.   Chen, F. *et al.* Nanoscale imaging of RNA with expansion microscopy. *Nat. Methods*

689   **13**, 679–684 (2016).

690   14.   Gao, R. *et al.* Cortical column and whole-brain imaging with molecular contrast and

691   nanoscale resolution. *Science (80-.).* **363**, eaau8302 (2019).

692   15.   Cahoon, C. K. *et al.* Superresolution expansion microscopy reveals the three-

693   dimensional organization of the *Drosophila* synaptonemal complex. *Proc. Natl. Acad. Sci.*

694   201705623 (2017). doi:10.1073/pnas.1705623114

695   16.   Halpern, A. R., Alas, G. C. M., Chozinski, T. J., Paredez, A. R. & Vaughan, J. C.

696   Hybrid Structured Illumination Expansion Microscopy Reveals Microbial Cytoskeleton

697   Organization. *ACS Nano* **11**, 12677–12686 (2017).

698   17.   Gao, M. *et al.* Expansion Stimulated Emission Depletion Microscopy (ExSTED).

699   *ACS Nano* **12**, 4178–4185 (2018).

700   18.   Xu, H. *et al.* Molecular organization of mammalian meiotic chromosome axis

701   revealed by expansion STORM microscopy. *Proc. Natl. Acad. Sci.* **116**, 18423–18428

702   (2019).

703   19.   Mahecic, D., Testa, I., Griffié, J. & Manley, S. Strategies for increasing the

704   throughput of super-resolution microscopies. *Curr. Opin. Chem. Biol.* **51**, 84–91 (2019).

705   20.   Sacconi, L. *et al.* Multiphoton multifocal microscopy exploiting a diffractive optical

706   element. *Opt. Lett.* **28**, 1918 (2003).

707   21.   Coelho, S. *et al.* Multifocal multiphoton microscopy with adaptive optical correction.

708   *Multiphot. Microsc. Biomed. Sci. XIII* **8588**, 858817 (2013).

709   22.   Cooper, D. J. F. Imaging distal end of multimode fiber. *United States Pat.* **1**, (2014).

710   23.   Nielsen, T., Fricke, M., Hellweg, D. & Andresen, P. High efficiency beam splitter for

711   multifocal multiphoton microscopy. *J. Microsc.* **201**, 368–376 (2001).

712   24.   Voelkel, R., Herzig, H. P., Nussbaum, P., Daendliker, R. & Hugle, W. B. Microlens

713   array imaging system for photolithography. *Soc. Photo-Optical Instrum. Eng.* **35**, 3323–

714   3330 (1996).

715   25.   Zimmermann, M., Lindlein, N., Voelkel, R. & Weible, K. J. Microlens laser beam

716   homogenizer: from theory to application. **666302**, 666302 (2007).

717   26.   Voelkel, R. & Weible, K. J. Laser beam homogenizing: limitations and constraints.

718   71020J (2008). doi:10.1117/12.799400

719   27.   Schreiber, P., Kudaev, S., Dannberg, P. & Zeitner, U. D. Homogeneous LED-

720   illumination using microlens arrays. *Nonimaging Opt. Effic. Illum. Syst. II* **5942**, 59420K

721   (2005).

722   28.   Model, M. A. & Blank, J. L. Concentrated dyes as a source of two-dimensional

723   fluorescent field for characterization of a confocal microscope. *J. Microsc.* **229**, 12–16

724   (2008).

725   29.   Curd, A. *et al.* Construction of an instant structured illumination microscope.

726   *Methods* **88**, 37–47 (2015).

727   30.   Friedman, J. R. *et al.* ER tubules mark sites of mitochondrial division. *Science (80-.*

728   *).* **334**, 358–362 (2011).

729   31.   Gambarotto, D. *et al.* Imaging cellular ultrastructures using expansion microscopy

730   (U-ExM). *Nat. Methods* 1 (2018). doi:10.1038/s41592-018-0238-1

731   32.   Görlitz, F. *et al.* easySLM-STED: Stimulated emission depletion microscopy with

732   aberration correction, extended field of view and multiple beam scanning. *J. Biophotonics*

733   **11**, 1–11 (2018).

734   33.   Guichard, P., Chrétien, D., Marco, S. & Tassin, A. M. Procentriole assembly

735   revealed by cryo-electron tomography. *EMBO J.* **29**, 1565–1572 (2010).

736   34.   Banterle, N. & Gönczy, P. Centriole Biogenesis: From Identifying the Characters to

737   Understanding the Plot. *Annu. Rev. Cell Dev. Biol.* **33**, 23–49 (2017).

738   35.   Janke, C. & Bulinski, J. C. Post-translational regulation of the microtubule

739   cytoskeleton: Mechanisms and functions. *Nat. Rev. Mol. Cell Biol.* **12**, 773–786 (2011).

740   36.   Bobinnec, Y. *et al.* Centriole disassembly in vivo and its effect on centrosome

741   structure and function in vertebrate cells. *J. Cell Biol.* **143**, 1575–1589 (1998).

742   37.   Xu, Z. *et al.* Microtubules acquire resistance from mechanical breakage through

743   intralumenal acetylation. *Science (80-.).* **356**, 328–332 (2017).

744   38.   Portran, D., Schaedel, L., Xu, Z., Théry, M. & Nachury, M. V. Tubulin acetylation

745   protects long-lived microtubules against mechanical ageing. *Nat. Cell Biol.* **19**, 391–398

746   (2017).

747   39.   Eshun-Wilson, L. *et al.* Effects of α-tubulin acetylation on microtubule structure and

748   stability. *Proc. Natl. Acad. Sci. U. S. A.* **116**, 10366–10371 (2019).

749   40.   Wolff, A. *et al.* Distribution of glutamylated alpha and beta-tubulin in mouse tissues

750   using a specific monoclonal antibody, GT335. *Eur. J. Cell Biol.* **59**, 425–32 (1992).

751   41.   Abal, M., Keryer, G. & Bornens, M. Centrioles resist forces applied on centrosomes

752   during G2/M transition. *Biol. Cell* **97**, 425–434 (2005).

753   42.   Hamel, V. *et al.* Identification of Chlamydomonas Central Core Centriolar Proteins

754   Reveals a Role for Human WDR90 in Ciliogenesis. *Curr. Biol.* **27**, 2486-2498.e6 (2017).

755   43.   Bobinnec, Y. *et al.* Glutamylation of centriole and cytoplasmic tubulin in proliferating

756   non- neuronal cells. *Cell Motil. Cytoskeleton* **39**, 223–232 (1998).

757   44.   Fortun, D. *et al.* Reconstruction from multiple particles for 3D isotropic resolution in

758   fluorescence microscopy. *IEEE Trans. Med. Imaging* **37**, 1235–1246 (2018).

759   45.   Sieben, C., Banterle, N., Douglass, K. M., Gönczy, P. & Manley, S. Multicolor single-

760   particle reconstruction of protein complexes. *Nat. Methods* **15**, 777–780 (2018).

761   46.   Campbell, M. G., Veesler, D., Cheng, A., Potter, C. S. & Carragher, B. 2.8 Å

762   Resolution Reconstruction of the Thermoplasma Acidophilum 20 S Proteasome Using

763   Cryo-Electron Microscopy. *Elife* **2015**, 1–22 (2015).

764   47.   Jiang, J., Pentelute, B. L., Collier, R. J. & Hong Zhou, Z. Atomic structure of anthrax

765   protective antigen pore elucidates toxin translocation. *Nature* **521**, 545–549 (2015).

766   48.   Meehl, J. B., Bayless, B. A., Giddings, T. H., Pearson, C. G. & Winey, M.

767   Tetrahymena Poc1 ensures proper intertriplet microtubule linkages to maintain basal body

768   integrity. *Mol. Biol. Cell* **27**, 2394–2403 (2016).

769 49.   Edelstein, A. D. *et al.* Advanced methods of microscope control using µManager

770   software. *J. Biol. Methods* **1**, 10 (2014).

771 50.   Schindelin, J. *et al.* Fiji: An open-source platform for biological-image analysis. *Nat.*

772   *Methods* **9**, 676–682 (2012).

773 51.   Klena, N. *et al.* Isolation and Fluorescence Imaging for Single-particle

774   Reconstruction of Chlamydomonas Centrioles. *J. Vis. Exp.* (2018).

775 52.   Wong, Y. L. *et al.* Reversible centriole depletion with an inhibitor of Polo-like kinase

776   4. *Science* **348**, 1155–1160 (2015)..